Small Structures

small structures

www.small-structures.com

RESEARCH ARTICLE OPEN ACCESS

Effects of Cu Surface Area and Microtexture on Lithium Plating in Anode-Less Batteries

Nassima Yamini[1,2] | Vincenzina Siciliani[3] | Biagio Anderlini[1] | Riccardo Pelaccia[3] | Marco Borsari[1] | Leonardo Orazi[3] | Andrea Mescola[4] | Francesco De Boni[5] | Matteo Lorenzoni[5] | Abdolkhaled Mohammedi[2] | Tommaso Iarocci[2] | Luca Bertoli[2] | Palanivel Molaiyan[6] | Michal Piszcz[2] | Michel Armand[7] | Vincent Giordani[2] | Andrea Paolella[1]

[1]Dipartimento di Scienze Chimiche e Geologiche, Università degli Studi Modena e Reggio Emilia, Modena, Italy | [2]Basquevolt, Alava Technology Park, Vitoria-Gasteiz, Spain | [3]Dipartimento di Scienze e Metodi per l'Ingegneria, Università degli Studi Modena e Reggio Emilia, Reggio Emilia, Italy | [4]Istituto Nanoscienze, Consiglio Nazionale delle Ricerche, Modena, Italy | [5]Materials Characterization Facility, Istituto Italiano di Tecnologia, Genova, Italy | [6]Research Unit of Sustainable Chemistry, University of Oulu, Oulu, Finland | [7]Università CIC Energigune Alava Technology Park, Vitoria-Gasteiz, Spain

Correspondence: Vincent Giordani (vgiordani@basquevolt.com) | Andrea Paolella (andrea.paolella@unimore.it)

Received: 29 January 2026 | **Revised:** 6 March 2026 | **Accepted:** 16 March 2026

Keywords: anode-less lithium batteries | copper oxide | current collector | microstructure | surface area

ABSTRACT

Anode-less lithium metal battery (ALLMB) technology relies on the development of current collectors capable of efficiently hosting metallic lithium during cycling. This work investigate in depth the role of surface area and microtexture in governing the lithium plating process, with particular attention to how surface texturing interacts in the presence of an interlayer on copper substrates. The study systematically examines the correlation between laser-induced surface modifications and the formation of a Cu_2O interlayer, aiming to clarify how these factors influence nucleation behavior and lithium deposition uniformity. The results reveal that the naturally formed Cu_2O interlayer on copper significantly masks the beneficial effects of a 3D textured surface, leading to plating behavior that was unexpectedly more favorable on a planar, 2D structure. In contrast, when the interlayer is removed, the intrinsic advantages of the 3D architecture become evident, resulting in markedly improved plating performance compared to its 2D counterpart. Overall, the findings highlight the critical importance of controlling both surface chemistry and microstructural design in anode-less configurations. Understanding the interplay between texturing and interlayer formation provides valuable insights for optimizing current collector engineering and achieving more stable and efficient lithium metal deposition.

1 | Introduction

The accelerating adoption of renewable energy and electric vehicles (EVs) demands better batteries with higher energy density and lower cost. While lithium-ion batteries (LIBs) combine efficiency and long life [1, 2], their graphite anodes (372 mAh g^{-1}) are nearing the theoretical limit of ~350 Wh kg^{-1} [2–4], and lithium supplies are increasingly constrained [5, 6]. Zero-excess lithium batteries, also known as anode-less lithium metal batteries (ALLMBs) have emerged as a promising alternative [7]. Rather than using thick lithium foils, which are costly, fragile and reactive [8, 9], ALLMBs pair a fully lithiated cathode with a current collector. During the first charge, lithium ions are removed from the cathode and plated onto the collector [10, 11]. Removing the heavy metal anode reduces cell mass and volume, increasing energy density by 40%–60% and simplifying production [12]. Because metallic lithium is absent at assembly, the cells are safer and easier to transport [12–15], and the design is compatible with existing LIB manufacturing lines, lowering costs and facilitating scale-up [1, 7, 15, 16]. Beyond improved energy density, anode-free batteries offer practical manufacturing and safety benefits. The absence of a

Nassima Yamini and Vincenzina Siciliani contributed equally to this work.

This is an open access article under the terms of the Creative Commons Attribution License, which permits use, distribution and reproduction in any medium, provided the original work is properly cited.

© 2026 The Author(s). *Small Structures* published by Wiley-VCH GmbH.

lithium metal foil eliminates the complex steps of synthesizing, handling and coating a highly reactive material. Instead, a thin copper collector is employed, thereby reducing the electrode's weight and facilitating fabrication. This reduced mass not only increases gravimetric energy density but also lowers material and processing costs. Because the cell contains no metallic lithium until it is first charged, it poses fewer hazards during shipping and assembly [5, 17–19]. However, this great advantage introduces a downside: there is no reservoir of lithium to compensate for side reactions or inefficiencies. The benefits of ALLMBs are balanced by serious challenges. With no excess lithium reservoir, the cell's life depends on nearly perfect lithium cycling. Any loss of lithium to solid-electrolyte interphase (SEI) formation or dead lithium quickly translates into capacity fade, making ALLMB performance highly sensitive to interfacial stability [18, 20]. Recent reports have demonstrated that electrolyte solvation regulation and interfacial engineering can dramatically enhance lithium reversibility even under extreme conditions, such as −40°C operation in silicon-based and aluminum-foil-based systems [21, 22]. A fresh SEI forms each time lithium is deposited and stripped, consuming lithium and electrolyte and accelerating capacity fade [23–27]. Recent advances are driving progress toward the practical realization of ALLMBs. Machine-learning algorithms accelerate electrolyte discovery by efficiently identifying high-performance formulations, while high-resolution imaging shows that pressure distribution strongly affects lithium microstructure, guiding improved collectors and formation designs. Similarly, anode-free sodium metal systems have demonstrated stable cycling at subzero temperatures through electrolyte and interfacial optimization, underscoring the universal importance of interface regulation in metal-free configurations [25]. Together, materials engineering and data science tackle the strict interfacial demands of anode-less systems [18, 28]. In summary, ALLMBs are able to eliminate the over-stoichiometric lithium anode, maximize energy density, and enhance safety, though their success depends on suppressing dendrite growth, stabilizing the SEI, and maintaining lithium inventory. Continued refinement of interfaces, electrolyte chemistry, and operating conditions is key to unlocking durable, high-energy ALLMBs for future energy storage [29]. Lithium metal must plate and strip from the copper collector with negligible loss. However, the bare copper surface leads to high local current densities and uneven deposition, fostering dendritic lithium that detaches as dead lithium and quickly exhausts the limited inventory [30, 31]. In these conditions, achieving coulombic efficiencies above 99.99 % is crucial [23, 26, 32]. Designing a new generation of current collectors is crucial to mitigate lithium metal plating issues. High-surface-area porous scaffolds, such as Cu foams, distribute current evenly, provide numerous nucleation sites and space to accommodate volume changes, thereby suppressing dendrite growth and maintaining high coulombic efficiency (CE) [29, 32–41]. For example, 3D structures with lithiophilic coatings like Ag or Au reduce nucleation overpotential and guide uniform lithium deposition; moderate coating thickness is important to avoid excessive alloying or dead lithium formation [42]. Careful design balances surface area, porosity and coating to lower current density without causing side reactions [43]. The optimization of electrolytes and salts, synergistically combined with functional coatings and current collector engineering, together with precise control of pressure, temperature, and current density, promotes stable SEI formation and uniform lithium metal deposition, thereby enhancing CE and cycle life while suppressing dendrite growth [1, 12, 43–47]. Building on the synergy between coating chemistry and operating conditions, anode-free systems increasingly rely on 3D current collectors to manage lithium metal plating. 3D scaffolds such as foams, meshes, and nanofibre networks expand the electroactive surface and lower local current density, accommodating volume changes during plating/stripping and promoting uniform lithium deposition. For example, Ag-coated copper foams prepared by polyol reduction combine high-surface area with a lithiophilic interface and deliver ~92% capacity retention after 100 cycles because the Ag coating induces uniform lithium nucleation [48]. However, a larger surface area also accelerates electrolyte decomposition; reviews highlight that 3D porous collectors reduce the effective current density but can cause more side reactions unless paired with suitable surface treatments [10, 31, 49]. In orderto overcome this limitation, researchers predeposit noble metals onto copper foams or meshes. Gold-covered 3D Cu collectors exhibit the lowest lithium nucleation overpotential (~6.5 mV) and maintain high CE over 100 cycles [10, 50]. Super-3D copper meshes derived from resorcinol–formaldehyde coatings store lithium within CuO_x-filled pores, achieving ~60% capacity retention and nearly full CE. Ultralight nanofibre networks offer even greater surface area and reduce nucleation energy, supporting dendrite-free, dense lithium layers and improving cycling stability [10]. Nevertheless, excessive lithiophilicity or coating thickness can consume active lithium; paper-based collectors with moderate Ag or Cu coatings strike a balance by forming stable SEI and limiting lithium depletion [51]. These examples underscore that 3D architectures, combined with tailored coatings and electrolyte optimization, are central to achieving durable anode-less batteries.

In this context, our findings indicate that a simple reduction in surface current density is not sufficient to enhance cell performance. Even when the apparent current per unit area is reduced by increasing the copper current collector area via laser-textured 3D architectures, performance can still deteriorate. This behavior highlights that such 3D structures do not inherently confer advantages as long as the native oxide layer remains intact, which hinders uniform interfacial processes and limits effective SEI formation. These results underscore the critical importance of current distribution and interfacial chemistry, suggesting that 3D architectures may become beneficial only when coupled with a more suitable interlayer capable of mitigating oxide-related limitations and stabilizing the electrode–electrolyte interface.

2 | Results and Discussion

An initial comparison between the surface of untreated 2D copper (Cu2D) **(a)** and 3D copper treated under different laser conditions, namely laser induced periodic surface structures (LIPSS) **(d)**, and parallel grooves (GR5) **(g)**, is shown in Figure 1. The untreated 2D Cu sample has its own intrinsic roughness, as can be seen from the images shown in Figure 1a–c. The LIPSS structures are clearly visible in the optical and scanning electron microscopy (SEM) images in Figure 1d–f, while the parallel grooves are visible in Figure 1g–i. In detail, LIPSS show a pitch of approximately 1 μm and a uniform structure over large areas. Further fine-tuning of the laser parameters can improve the regularity of the structures and the presence of deposited nanoparticles, which do not drastically affect the induced roughness. The depth reached in the grooves' texture is estimated through

26884062, 2026, 4, Downloaded from https://onlinelibrary.wiley.com/doi/10.1002/sstr.202600021 by CochraneItalia, Wiley Online Library on [18/04/2026]. See the Terms and Conditions (https://onlinelibrary.wiley.com/terms-and-conditions) on Wiley Online Library for rules of use; OA articles are governed by the applicable Creative Commons License

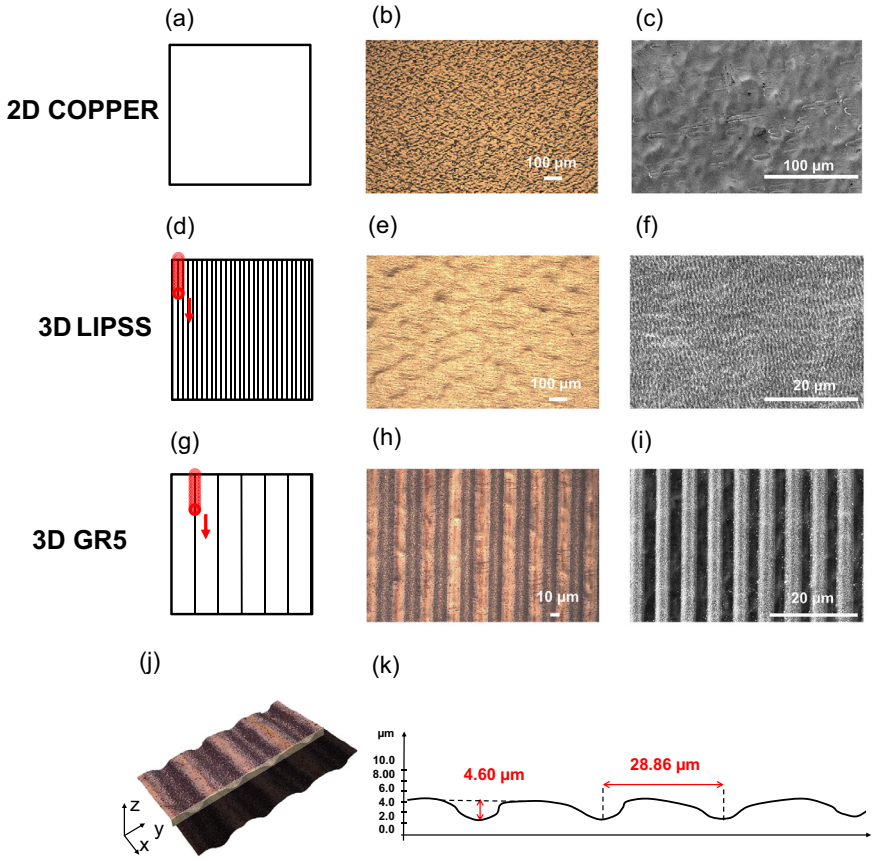

FIGURE 1 | Schematic representation of the laser textures analyzed, with respect to the untreated 2D material (a): (d) micrometric LIPSS; (g) micrometric grooves GR5; (b,e,h) optical microscope images; (c,f,i) SEM microscope images; and (j,k) GR5 3D profile at digital microscope.

profilometer scans, as shown in Figure 1j–k: it reaches approximately an average of 5 µm. The exact depth of the LIPSS cannot be detected in detail by the profilometer because the sensitivity of the instrument with the available lenses is comparable to the size of the structures themselves, see Figure S1 . Therefore, only for the sample with LIPSS, atomic force microscopy (AFM) analyses were performed, confirming the periodicity of the structures at approximately 1 µm and a depth of approximately 70 nm, see Figure S2.

Anode-less Cu||LFP coin cells were cycled while varying the imposed cyclable lithium inventory by limiting the charge capacity to 0.5, 1.0, 1.8, or 2.5 mAh cm^{-2} (Figure 2a–d; see Methods and Supporting Information (SI) for protocol details). Across all areal capacities, Cu2D consistently delivers the longest cycle life and highest capacity retention, outperforming both 3D-textured current collectors (GR5 and LIPSS) by ~10% in lifetime under these conditions.

Notably, the GR5 and LIPSS surfaces—which have increased roughness and surface area—show the shortest cycle lifetimes in this capacity range, indicating that excessive surface area is detrimental under these conditions. Interestingly, in all cases, the CE improves as the plated lithium metal capacity is raised from 0.5 to 2.5 mAh cm^{-2}. This trend is explained by the larger absolute amount of lithium metal deposited at 2.5 mAh. A higher lithium inventory per cycle reduces the relative fraction of lithium becoming "dead" (electrochemically inactive) during stripping, thereby raising the CE [11, 30, 52].

In order to investigate whether this arises from a change in lithium microstructure, ex situ SEM was conducted on LIPSS samples plated at 0.25 and 2.0 mAh cm^{-2} (Figure 2f,g). The images reveal a transition from a high-surface-area whisker/moss-like deposit at low capacity to a denser, lower-surface-area morphology at high capacity. We attribute this capacity-dependent morphology shift primarily to increasing stack constraint/pressure as plated lithium thickness grows within the confined coin-cell geometry, which promotes coalescence and densification of the deposit at higher capacities [53]. This reduced surface area is consistent with improved stripping efficiency and lower parasitic consumption, thereby contributing to the observed increase in CE at higher plated capacities. Overall, the smoother Cu2D collector promotes more uniform lithium deposition/stripping and minimizes isolated Li, whereas rougher 3D structures favor inhomogeneous plating that leaves behind more electrically isolated Li. However, we note that even when the structure approaches saturation (Figure S10), the initial nucleation homogeneity induced by the 3D texture continues to influence stripping reversibility and lithium utilization. Consistently, the GR5 sample (moderate roughness) outperforms the higher-surface-area LIPSS in both capacity retention and CE, underscoring that an overly rough Cu current collector can accelerate loss of cyclable lithium metal in anode-less Li-metal cells. The impedance measures reported in Figure 3 can offer some interesting insights into the underlying reason.

Electrochemical impedance spectroscopy (EIS) measurements were performed on lithium metal coin cells using 4 M lithium bis (trifluoromethanesulfonyl)imide in dimethyl ether (LiFSI/DME) electrolyte and Cu2D, GR5, or LIPSS-structured Cu current collectors after an increasing number of charge–discharge cycles,

26884062, 2026, 4, Downloaded from https://onlinelibrary.wiley.com/doi/10.1002/sstr.202600021 by CochraneItalia, Wiley Online Library on [18/04/2026]. See the Terms and Conditions (https://onlinelibrary.wiley.com/terms-and-conditions) on Wiley Online Library for rules of use; OA articles are governed by the applicable Creative Commons License

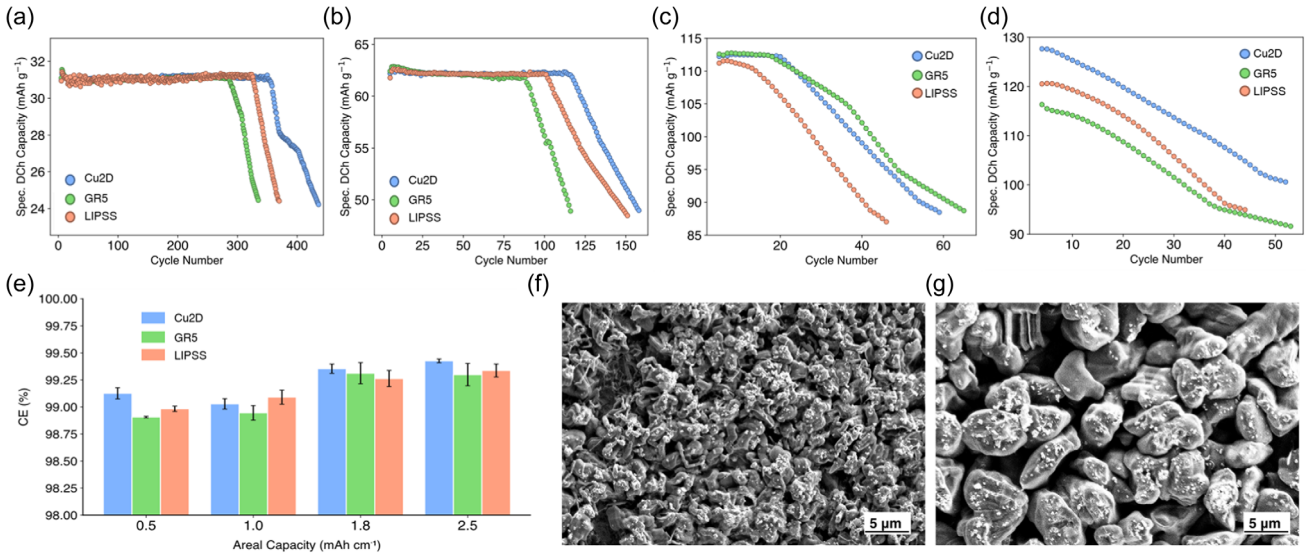

FIGURE 2 | Electrochemical performance and morphology trends of Cu2D and laser-textured Cu current collectors in anode-free Cu||$LiFePO_4$ (LFP, loading = 2.5 mAh cm^{-2}) cells as a function of imposed plated capacity (current density = C/3 (0.833 mA cm^{-2}) – 1D (2.5 mA cm^{-2})). Representative cycling performance at the following plated capacities specifically 0.5 mAh cm^{-2} (a), 1.0 mAh cm^{-2} (b), 1.8 mAh cm^{-2} (c), 2.5 mAh cm^{-2} (d, full capacity). (see Methods for protocol details). (e) Average CE for each current collector across the tested capacities, values averaged over three independent coin cells. (f,g) Representative ex situ SEM images of lithium plated on LIPSS copper after depositing 0.25 mAh cm^{-2} (f) and 2.0 mAh cm^{-2} (g), showing a transition from a high-surface-area whisker/moss-like deposit at low capacity to a denser, lower-surface-area morphology at high capacity.

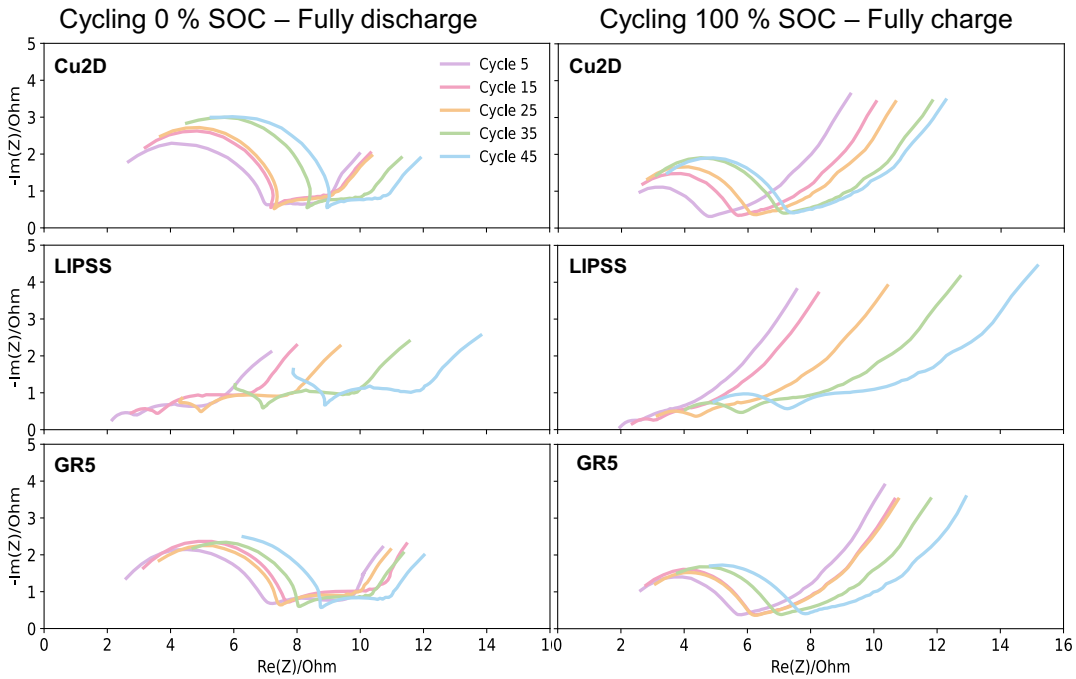

FIGURE 3 | Nyquist plots of the Cu2D, GR5, and LIPSS samples both in 0% and 100% SOC.

both at 0% and 100% state of charge (SOC) (Figure 3). The Nyquist plots are qualitatively similar across samples and SOC conditions, exhibiting multiple impedance contributions associated with interfacial processes at the lithium metal electrode.

At high frequencies, a well-defined semicircle is observed for Cu2D and GR5 electrodes at both SOCs at increasing the number of charge/discharge cycles. This feature is commonly attributed to the charge–transfer resistance in parallel with the transport properties of the inner SEI and reflects the dominant kinetics of lithium plating and stripping [54, 55]. The diameter of this semicircle provides insight into the activation barriers and interfacial stability of the lithium electrode. At early cycling stages, laser-structured collectors (particularly the LIPSS sample) exhibit a reduced high-frequency semicircle diameter, indicating lower initial interfacial resistance. This behavior is especially evident at 0% SOC and can be attributed to a more homogeneous current distribution and enhanced electrolyte wettability resulting from the increased surface area of the structured collectors. However,

26884062, 2026, 4, Downloaded from https://onlinelibrary.wiley.com/doi/10.1002/sstr.202600021 by CochraneItalia, Wiley Online Library on [18/04/2026]. See the Terms and Conditions (https://onlinelibrary.wiley.com/terms-and-conditions) on Wiley Online Library for rules of use; OA articles are governed by the applicable Creative Commons License

upon continued cycling, the diameter of the high-frequency semicircle progressively increases for all samples, with a more pronounced growth observed for the structured collectors compared to Cu2D. This evolution indicates an accelerated increase in interfacial resistance and a gradual degradation of the active surface [54]. Thus, while Cu2D initially exhibits a slightly higher interfacial resistance due to its lower surface area, lithium deposited on high-surface-area collectors such as LIPSS progressively evolves toward a more resistive state during cycling, indicating that the same high-surface area that initially facilitates charge transfer also amplifies interfacial degradation processes and ultimately offsets the initial kinetic advantage.

At medium frequencies, an additional depressed semicircle emerges after approximately five charge–discharge cycles, becoming increasingly evident with continued cycling. This contribution is associated with the development of a secondary interfacial process characterized by a shorter time constant than the primary charge–transfer/inner SEI response. In LiFSI/DME systems, this behavior is well-known and is attributed to the progressive formation of a multilayer SEI [56, 57]. Repeated stripping and plating of lithium expose fresh metallic lithium, causing continuous SEI rupture and reformation. This leads to the buildup of an outer SEI layer composed of salt-derived and solvent-derived degradation products (e.g., LiF-rich and organic components), which is more resistive and structurally heterogeneous than the initial inner SEI. As cycling proceeds, this outer SEI grows thicker and more disordered, producing an increasingly distinct semicircle in the Nyquist plot. Its amplification over cycles therefore serves as a clear electrochemical signature of interfacial degradation and SEI instability in ether-based electrolytes without stabilizing additives. The result is consistent with literature reports on lithium metal anodes in LiFSI/DME, which frequently exhibit separation of time constants corresponding to inner versus outer SEI layers [56, 57]. Overall, the observed semicircle growth reflects progressive SEI evolution and increased surface resistance, highlighting the inherent instability of the lithium metal surface under these electrolyte conditions.

At low frequencies, the impedance response transitions into a Warburg-like region, characterized by an approximately linear tail with a slope close to 45°, indicative of diffusion-controlled transport of Li^+ ions through the SEI and electrolyte. Deviations from an ideal Warburg behavior suggest increasing mass-transport limitations, potentially arising from evolving surface morphology and partial pore blocking during cycling [58].

The LIPSS-structured electrodes exhibit a more complex impedance response, particularly at high and medium frequencies. LIPSS samples Nyquist plots display multiple depressed semicircles, reflecting a distribution of interfacial time constants. This behavior originates from the nanoscale ridges and grooves introduced by laser-induced periodic surface structuring (LIPSS), which generate significant morphological and energetic heterogeneity across the electrode surface. Local variations in curvature and surface energy lead to nonuniform lithium nucleation, SEI formation, and charge–transfer kinetics, resulting in spatially distributed interfacial processes detectable by EIS [54]. Despite this complexity, the low-frequency Warburg response remains comparable to that of the other samples, indicating that bulk ionic diffusion is not significantly affected by surface patterning. Overall, these EIS results demonstrate that while laser structuring (especially LIPSS) reduces the initial interfacial resistance and enhances early-stage kinetics, it also accelerates interfacial degradation upon cycling. This interpretation is consistent with the spontaneous impedance increase observed during electrolyte soaking, indicating that surface-driven parasitic reactions precede and subsequently exacerbate electrochemical degradation. Consequently, the interfacial instability revealed by EIS provides a microscopic origin for the faster resistance growth and performance decay observed during prolonged cycling.

Since interfacial degradation is ultimately governed by the morphology of plated lithium, ex situ SEM was employed to directly probe lithium deposition on the different Cu current collectors. Figure 4 presents SEM images comparing lithium deposition on three different CuCCs after galvanostatic plating at a limited areal capacity of 0.25 mAh cm^{-2}. For Cu2D (Figure 4a–c), lithium deposition is highly heterogeneous. Low-magnification images reveal isolated lithium islands that progressively evolve into irregular agglomerates. At higher magnification, a porous and mossy morphology with dendritic features is observed, indicating localized lithium nucleation and growth driven by nonuniform Li^+ flux and high local current density. The sample GR5 (Figure 4d–f) exhibits a modified deposition behavior; laser texturing partially guides lithium deposition along the patterned channels. While the grooves increase the effective surface area and act as preferential deposition sites, high-magnification images still reveal irregular lithium clusters and filament-like structures. This suggests that the relatively large spacing between grooves leaves extended flat regions where current density remains locally concentrated, limiting the overall homogenization of lithium growth.

In contrast, copper collector LIPSS (Figure 4g–i,) shows a markedly improved lithium deposition morphology. The periodic nanostructure leads to a continuous and compact lithium layer. High-resolution SEM images reveal densely packed, sub-micrometric nodules without evidence of dendritic growth. The dense network of nanoscale features provided by the LIPSS effectively increases the density of nucleation sites and reduces the local current density, promoting uniform, bottom-up lithium growth.

Although hierarchical micro- and nanostructuring promotes more uniform initial lithium nucleation even in the presence of surface oxides generated during laser processing, this early advantage does not always translate into improved long-term electrochemical performance. Laser surface treatments commonly lead not only to topographical patterning but also to the formation of copper oxides (such as CuO and Cu_2O) on the patterned surface due to localized heating and rapid reoxidation in ambient conditions. These laser-induced oxides create additional lithiophilic sites and increase surface roughness, which can facilitate lithium nucleation and temporarily reduce the nucleation overpotential, thereby partially homogenizing early deposition [59–61]. However, surface oxides typically possess lower electronic conductivity and can significantly influence the chemistry and morphology of the evolving SEI. The presence of an oxide layer (native or laser-generated) can dominate the evolving interface chemistry, leading to inhomogeneous SEI formation, increased parasitic side-reactions, and uneven local current density distribution during cycling [60]. As a result, the beneficial effect of structured topography on lithium plating morphology may be masked, and improvements in CE, capacity retention or long-term stability may not be observed (as shown by electrochemical results), despite the more uniform initial

26884062, 2026, 4, Downloaded from https://onlinelibrary.wiley.com/doi/10.1002/sstr.202600021 by CochraneItalia, Wiley Online Library on [18/04/2026]. See the Terms and Conditions (https://onlinelibrary.wiley.com/terms-and-conditions) on Wiley Online Library for rules of use; OA articles are governed by the applicable Creative Commons License

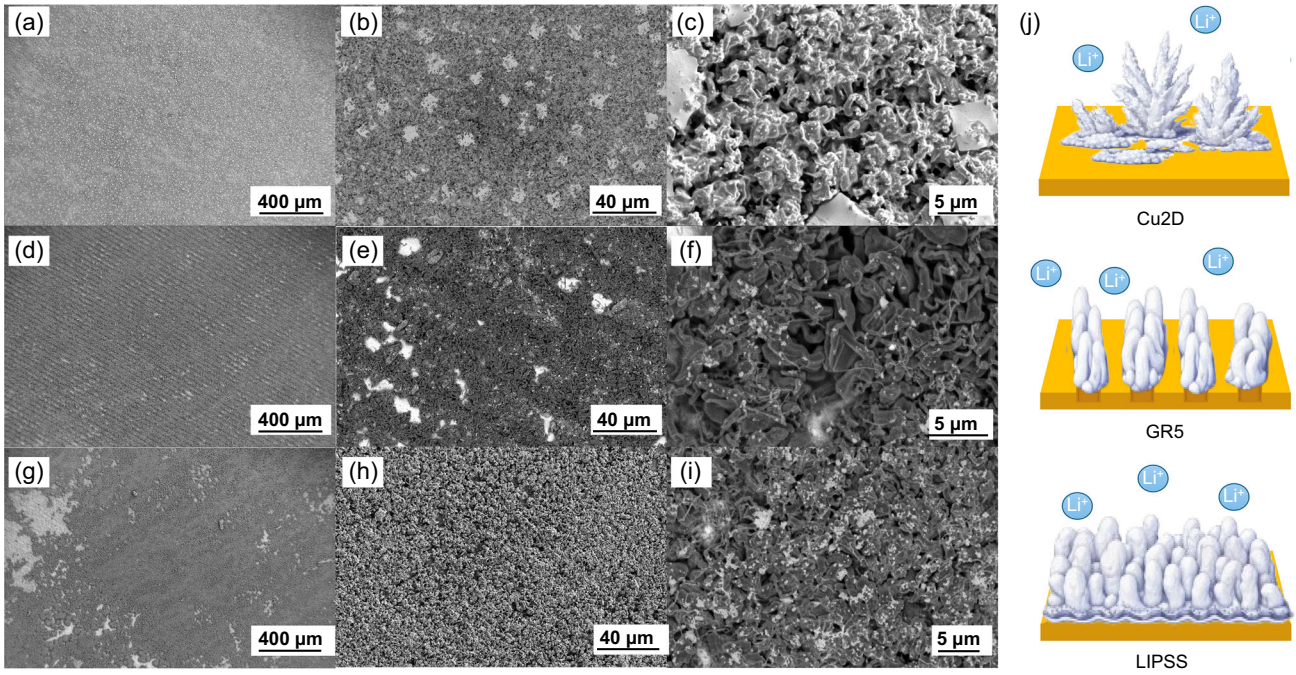

FIGURE 4 | SEM images of the Cu electrode surface at a limited Li-plated capacity of 0.25 mA cm^{-2}; samples **Cu2D** (a–c); **GR5** (d–f); **LIPSS** (g–i); and (j) schematic illustration of different lithium deposition morphologies for each CCs.

nucleation. This behavior highlights that while surface structuring enhances early lithium nucleation, electrochemical performance is fundamentally governed by the combined effects of surface topography and surface chemistry.

In order to completely rule out any potential influence originating from surface artifacts that might have formed as a consequence of the laser-processing step, we implemented an additional cleaning procedure aimed at removing the superficial oxide layer present on the different samples. This was accomplished by allowing the oxide to react with glucose, thereby selectively dissolving and lifting it from the surface; further operational details regarding this procedure can be found in the methods section.

As illustrated in Figure 5, our measurements clearly revealed that the sample exhibiting the largest effective surface area (namely, the deoxidized LIPSS (D_LIPSS)) demonstrated the most favorable electrochemical behavior. In particular, this sample showed the highest degree of capacity retention throughout cycling as well as the greatest CE, and these advantages were consistently observed regardless of the magnitude of the applied capacity. A closer look at the cycling curves highlights this superiority: D_LIPSS maintains a plateau in discharge capacity for ~150–180 cycles, whereas deoxidated Cu2D and GR5 collectors fail much earlier. When the plated capacity is increased to 2.5 mAh cm^{-2}, the advantage of D_LIPSS becomes even more evident, with the untreated samples fading after ~ 100 cycles while D_LIPSS retains high capacity and CE.

The bar chart summarizing the CE values shows that D_LIPSS consistently delivers a higher average CE (~99.5 %) than the other deoxidated collectors, indicating more reversible plating/stripping. This improved behavior arises because the deoxidation treatment removes the dark, native Cu_2O/CuO layer, exposing metallic Cu that reduces parasitic reactions and enables more uniform lithium nucleation; mechanistic studies have shown that the native copper oxides and their reduction products by lithium contribute to the SEI, leading to side reactions and poor CE, and that removing this layer via acid treatment alters the SEI composition and improves plating efficiency [62, 63]. In our system, eliminating the oxide layer also made it possible to expose the intrinsic effect of the 3D LIPSS topology, which indeed reduces local current density and homogenizes Li^+ flux [62]. However, although samples without native oxide–derived species exhibit a lower CE than untreated samples, the effect of the enhanced surface is visible when the native layer is removed. X-ray photoelectron spectroscopy (XPS) and X-ray diffraction (XRD) analyses of the samples before and after the oxide removal process are reported in the SI. Subsequently, the different copper samples were examined in greater detail to evaluate how their surfaces evolve as a function of the electrolyte's interaction over time. This analysis allowed us to isolate the intrinsic chemical reactivity of each surface morphology in the absence of any electrochemical bias.

As presented in Figure 6a, the Cu2D reference sample exhibits remarkably stable behavior when in direct contact with the electrolyte, showing no significant changes in its interfacial properties over the entire observation window (0 to 12 h). In contrast, the high-surface-area samples display a distinctly different evolution, even though no external current was applied during the test. Both LIPSS and GR5 undergo a measurable increase in internal resistance, indicating that their expanded surface areas facilitate enhanced, and likely undesirable, interactions with the electrolyte. This phenomenon strongly suggests that, as the effective surface area increases, the extent of spontaneous parasitic reactions also increases, ultimately degrading interfacial stability. Interestingly, when the samples are deoxidized prior to testing, their behavior changes considerably.

The deoxidized surfaces (as shown in Figure 6b) follow a more uniform trend across the different morphologies, displaying much closer similarities in their resistance evolution. This observation is indicative of a substantially reduced degree of reaction

26884062, 2026, 4, Downloaded from https://onlinelibrary.wiley.com/doi/10.1002/sstr.202600021 by CochraneItalia, Wiley Online Library on [18/04/2026]. See the Terms and Conditions (https://onlinelibrary.wiley.com/terms-and-conditions) on Wiley Online Library for rules of use; OA articles are governed by the applicable Creative Commons License

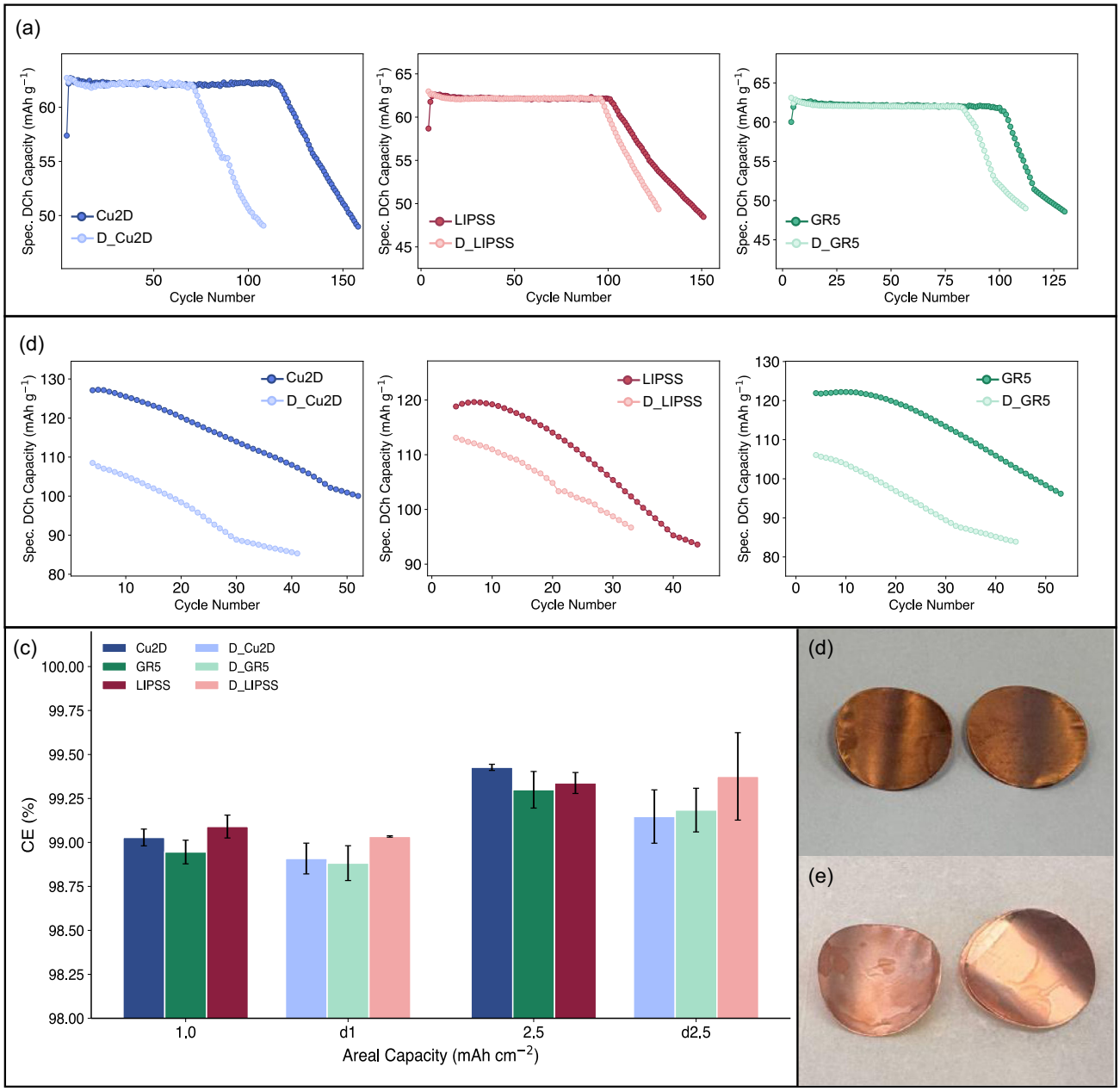

FIGURE 5 | Cycling performances and CE of deoxidated Cu bare and 3D CCs as anode in ALLMB $LiFePO_4$ (LFP, loading = 2.5 mAh cm^{-2}) cells with different capacities: (a) 1 mAh cm^{-2} and (b) 2.5 mAh cm^{-2}; (c) average CE for each current collector across the tested capacities, values averaged over three independent coin cells; 3D CC LIPSS before (d) and after (e) the deoxidation.

between the electrolyte and the underlying copper substrate once the surface oxide layer has been removed. Taken together, these findings imply that the copper-oxide interlayer itself plays a pivotal role in driving parasitic reactivity. When this oxide is spread across a high-surface-area structure, its chemical accessibility increases, making it far more susceptible to trigger electrolyte decomposition processes. Such reactions, in turn, contribute to a progressive change in interfacial resistance. These results highlight that roughness, and by extension, the total accessible surface area, must be carefully considered when analyzing or optimizing lithium metal plating mechanisms. The data also brings forward an important conceptual point: although the copper-oxide layer is known to be lithiophilic [64] and can therefore assist in initial lithium nucleation, it simultaneously acts as a source of electrolyte degradation, potentially through a Cu^+/Li^+ cation-exchange-driven decomposition pathway. This dual role underscores the complexity of surface engineering strategies for lithium-metal anodes and the need for a balanced design approach.

The Nyquist plots reported in Figure 6 clearly highlight the combined influence of current-collector morphology and surface chemistry on the interfacial electrochemical response. In all cases, the spectra consist of a depressed semicircle in the high-to-medium frequency region followed by a low-frequency tail, characteristic of interfacial polarization processes coupled with diffusion-related contributions. In the oxidized condition (Figure 6a), smooth copper exhibits the narrowest semicircle,

26884062, 2026, 4, Downloaded from https://onlinelibrary.wiley.com/doi/10.1002/sstr.202600021 by CochraneItalia, Wiley Online Library on [18/04/2026]. See the Terms and Conditions (https://onlinelibrary.wiley.com/terms-and-conditions) on Wiley Online Library for rules of use; OA articles are governed by the applicable Creative Commons License

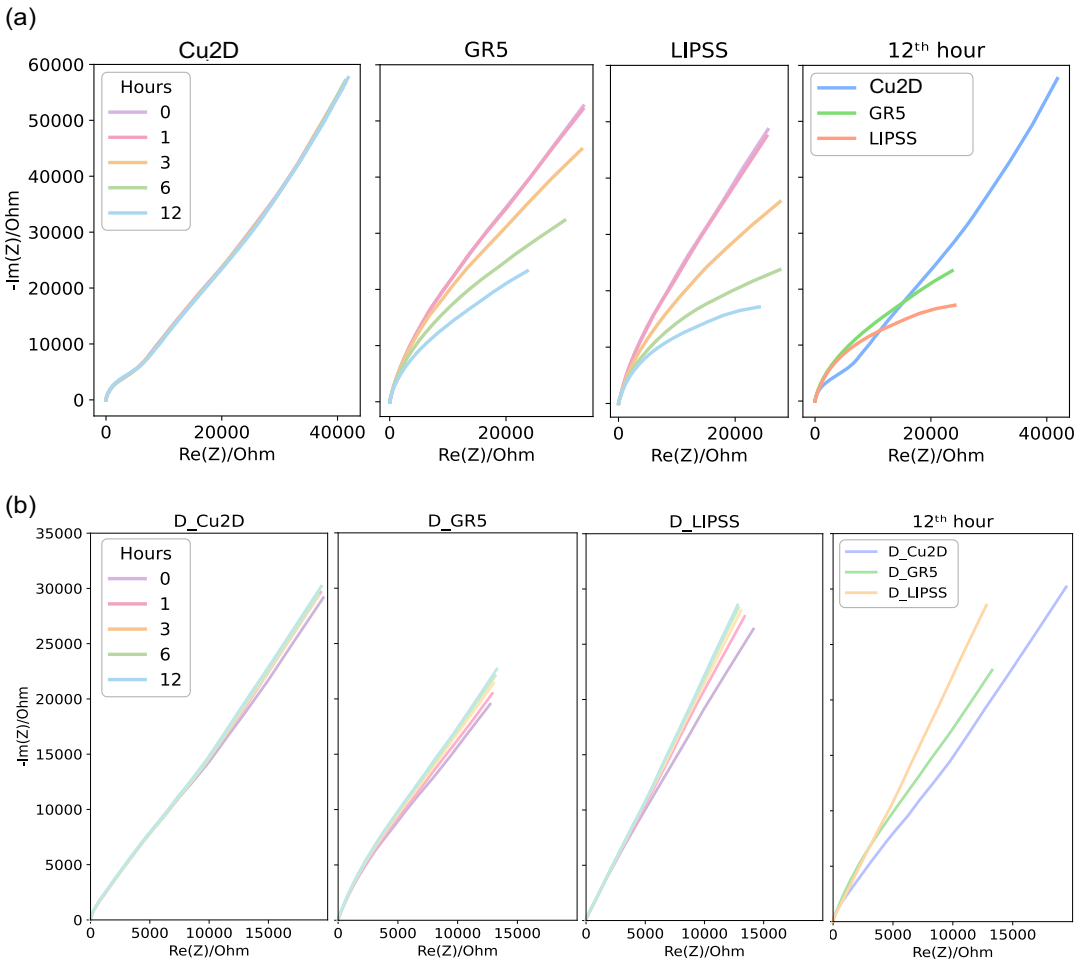

FIGURE 6 | Nyquist plots of the (a) Cu2D, GR5, LIPSS samples and (b) deoxidized samples during 12 h of wetting before cycling with focus on the 12th hour.

which is related to the different kinds and thicknesses of the surface oxide layer. The high-frequency intercept on the real axis, associated with the ohmic resistance of the electrolyte and cell components (R_s), is slightly higher for oxidized samples, with values of approximately 2.12 Ω for Cu2D, 2.08 Ω for GR5, and 1.65 Ω for LIPSS, reflecting the additional resistive contribution of the native surface layer. Since equivalent-circuit fitting was not performed, the resistance associated with the dominant semicircle was estimated directly from the Nyquist apex according to Equation (1), providing a qualitative metric for comparing interfacial polarization among samples. At the 12th hour, oxidized Cu2D displays the lowest interfacial arc resistance of approximately 8.87 kΩ, whereas the laser-structured collectors show significantly higher values, around 49.7 kΩ for GR5 and 44.1 kΩ for LIPSS (see the SI for additional information).

$$R_{arc} = 2(Re_{peak} - R_s) \quad (1)$$

The pronounced impedance observed for laser-treated samples is attributed to the presence of the thicker Cu_2O/CuO layer, which acts as a partially insulating and chemically heterogeneous interphase. Native or induced copper oxides are known to strongly affect the early stages of solid–electrolyte interphase formation, leading to a lithiophobic and inhomogeneous interface that increases polarization and impedance [62]. Moreover, increasing the surface resistivity of the current collector has been shown to alter lithium nucleation behavior and enhance interfacial polarization [65]. In this context, laser-induced surface structuring partially mitigates the detrimental effect of the oxide layer by increasing the effective electrochemically accessible area, a trend consistent with previous studies on structured copper current collectors reporting improved electrolyte wetting/contact and reduced polarization compared to flat Cu surfaces [30, 36, 60].

After oxide removal (Figure 6b), a marked reduction in interfacial impedance is observed for all samples. The ohmic resistance becomes more uniform and slightly lower than in the oxidized case, with R_s values of approximately 1.64 Ω for Cu2D, 1.34 Ω for GR5, and 1.37 Ω for LIPSS, indicating improved electrical contact at the interface. The semicircles disappear before formation, thus it is not possible to estimate the R_{arc}; this different behavior could be attributed to the absence of the oxide layer.

At low frequencies, the spectra retain a diffusion-related tail, indicative of mass-transport limitations. The laser-textured collectors exhibit a slightly more vertical low-frequency response compared to smooth copper, suggesting improved electrolyte accessibility and reduced concentration gradients at the electrode–electrolyte interface, in line with observations commonly reported for laser-textured current collectors [36]. Notably, the Nyquist curves of D_GR5 and D_LIPSS largely overlap at the 12th hour, indicating that once the oxide barrier is removed and the interphase is stabilized, the interfacial response

26884062, 2026, 4, Downloaded from https://onlinelibrary.wiley.com/doi/10.1002/sstr.202600021 by CochraneItalia, Wiley Online Library on [18/04/2026]. See the Terms and Conditions (https://onlinelibrary.wiley.com/terms-and-conditions) on Wiley Online Library for rules of use; OA articles are governed by the applicable Creative Commons License

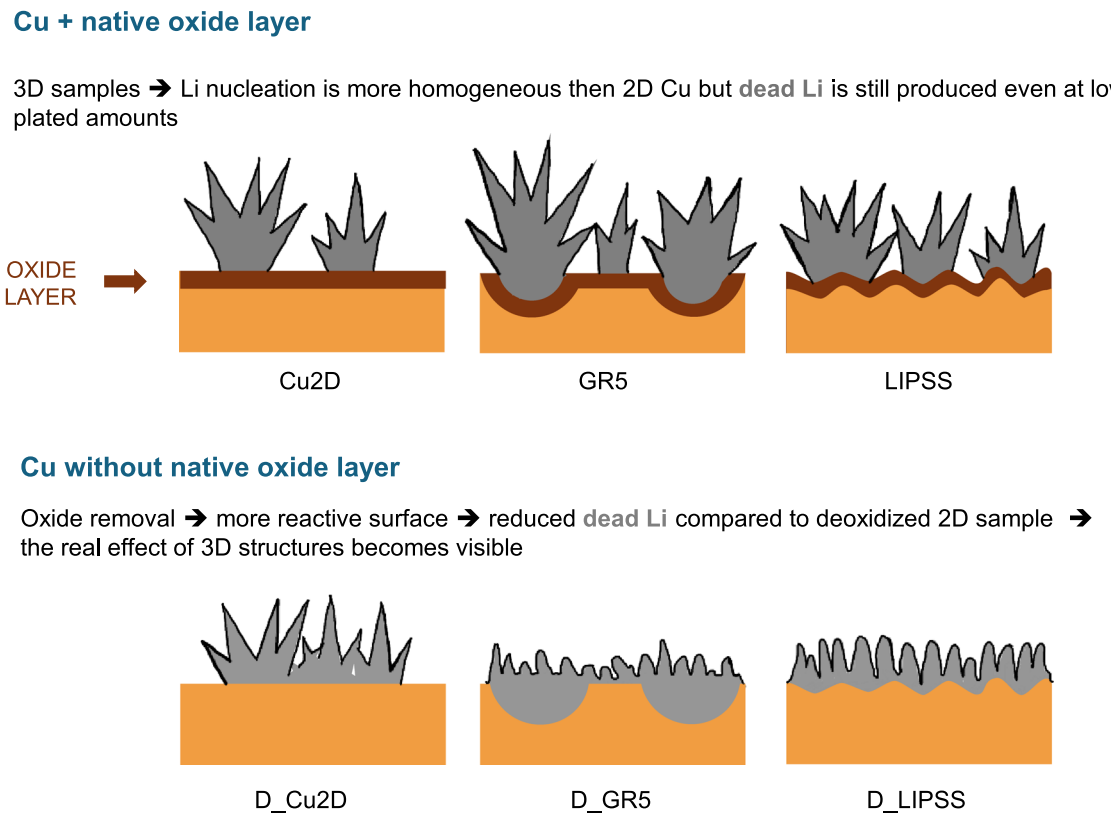

FIGURE 7 | Schematic representation of Li plating behavior in the samples before and after the deoxidation treatment in order to show that after the removal of the superficial oxide layer the real effect of 3D structures comes out.

is primarily governed by the increased active area provided by surface structuring rather than by subtle differences in surface morphology. Overall, the EIS analysis demonstrates that copper oxides strongly increase interfacial polarization, both native and laser-induced layers. The deoxidation strongly changes the EIS spectra for both 2D and 3D samples, confirming the critical role of surface chemistry and morphology in controlling the electrochemical behavior of Cu-CCs [30, 36, 60]. After the deoxidation, the chemical barrier is eliminated and the impedance response becomes primarily governed by surface structure, with laser-textured collectors exhibiting markedly reduced interfacial arc resistance compared to smooth copper.

The Figure 7 summarizes how lithium deposition evolves on the different collectors studied: laser-textured 3D surfaces, coupled with removal of the oxide film, guide plating toward compact and uniform deposits, reducing isolated lithium; by contrast, when the Cu_2O/CuO layer remains, the interface is lithiophobic and even the 3D structures do not prevent irregular deposits [66]. The beneficial effect of removing the oxide is amplified by the larger electroactive area of the 3D collectors, which, as shown in other work, favors current distribution and suppresses dendrite growth [67]. However, as discussed earlier, long-term stability also depends on the composition and homogeneity of the interphase: some surface species (for example, OH^- groups) can promote a more uniform SEI, while complete deoxidation does not always produce the desired outcome [62]. The final figure therefore, illustrates the potential of the processed and treated collectors but also prompts consideration of the complex interaction between topography, surface chemistry, and electrochemical conditions in determining overall cycling performance.

3 | Conclusions

The study provides a systematic assessment of how high-surface Cu CC correlates with the presence of a Cu_2O interlayer, with the goal of elucidating their combined influence on lithium nucleation and deposition uniformity. The findings show that the naturally occurring Cu_2O layer on copper largely suppresses the advantages typically offered by a 3D textured surface, ultimately promoting plating behavior that is more favorable on a flat, 2D substrate. Conversely, once the interlayer is removed, the inherent benefits of the 3D architecture become evident, yielding significantly improved plating performance relative to the two-dimensional counterpart. Collectively, these results underscore the crucial role of simultaneously managing surface chemistry and microstructural design in anode-less systems. This study provides new research insights: although Cu_2O is not the ideal interlayer for 3D Cu structures, alternative interlayers could be explored to preserve the benefits associated with high-surface area. A deeper understanding of the interactions between surface texturing and interlayer formation offers valuable guidance for the rational engineering of current collectors and for achieving more stable and efficient lithium metal deposition.

4 | Experimental Methods

4.1 | Copper Current Collectors

The substrate material is a commercial 10 μm copper coil (TMAX Battery Equipments, TMAX-DR01), generally used for electrodes. From this, samples in 60×40 mm dimensions were obtained,

26884062, 2026, 4, Downloaded from https://onlinelibrary.wiley.com/doi/10.1002/sstr.202600021 by CochraneItalia, Wiley Online Library on [18/04/2026]. See the Terms and Conditions (https://onlinelibrary.wiley.com/terms-and-conditions) on Wiley Online Library for rules of use; OA articles are governed by the applicable Creative Commons License

and they were treated for 30 min in a 0.1 M $(NaPO_3)_6$ solution at 50°C to remove any surface impurities and oxides. They were then sonicated for 5 min, rinsed with water and acetone, and stored in acetone during the experimental campaign. 14 mm discs were prepared using a cathode cutter from both the pure copper reference (Cu2D) and the laser-modified copper. After drying in an oven at 60°C, the samples were promptly moved into the glovebox.

4.2 | Electrolyte

The electrolyte was prepared from pure chemicals in an argon glovebox using a precision balance and pipette filler. The chemicals used include LiFSI, DME (Thermo Fisher Scientific, >99%). All steps, from preparation to use, were conducted under an inert atmosphere in the argon glovebox (H_2O, $O_2 < 0.1$ VPM).

4.3 | Laser Processing

The experimental laser setup includes an ultrashort-pulsed Ekspla Atlantic 50 laser source with a pulse duration of about 10 ps, equipped with three different wavelengths. To exploit the maximum power of the laser on copper, the wavelength of 1064 nm was employed. In addition, a Raylase Superscan V galvanometric scanning head precisely controls and directs the laser on the target, and an F-theta lens provides a focused beam with a waist diameter at $1/e^2$ intensity of about 10 μm. The two scanning strategies chosen are one micrometric and one sub-micrometric, as depicted in Figure 1. The first is a groove linear pattern realized with equally spaced parallel lines with a pitch of 30 μm with a depth of 5 μm (GR5). The second texture analyzed consists of the LIPSS. The parallel line texture was selected because it demonstrates the scalability of the process at an industrial level. In this setup, the sheet moves beneath the head while the laser scans it efficiently in a continuous motion, eliminating the need to jump between individual points. The laser parameters to ensure the design depths and good processing quality were: 1000 kHz of repetition rate, 30 μm line spacing, 2000 mm/s of scan speed, 4 passes, 8.7 W of power, corresponding at 8.7 μJ energy per pulse and 11.0 J cm^{-2} of fluence, for grooves; and 333 kHz of repetition rate, 4.5 μm line spacing, 1500 mm/s of scan speed, 3 passes, 0.85 W of power, corresponding at 0.85 μJ energy per pulse and 1.1 J cm^{-2} of fluence, see Table S1. The process parameters were chosen to impose the lowest possible heat input on the material without requiring long processing times, but they can be further optimized. For example, processing time for 39 x 39 mm^2 grooves is 2:30 min, for LIPSS texturing is 3:40 min.

4.4 | Coin-Cell Testing

CR2032-type coin cells were assembled in an argon-filled glovebox. The laser-modified Cu foils and Cu2D foils were used as current collectors on the anode side (14 mm Ø), while $LiFePO_4$ (12 mm Ø) electrodes served as the cathodes (Figure S3). Experiments were conducted under lean-electrolyte conditions, using 10 μL of 4 M LiFSI in DME as the electrolyte (Figure 2f). All cells were assembled in an anode-less configuration (Cu ‖ LFP) and tested at 25°C using a Neware battery cycler (Neware WHW-100L-2-0C-220V). After 24 h of wetting and Formation cells were cycled at 25°C, C/3. The theoretical capacity of $LiFePO_4$ was 2.5 mAh cm^{-2}: the plating was carried out by depositing different amounts of lithium, specifically 2.5 mAh cm^{-2} (full capacity), 1.8, 1, and 0.5 mAh cm^{-2}. Once the specified capacity was plated, all the available lithium was stripped by discharging the cell at 1C to the cutoff voltage of 2.8V, ensuring full stripping. The attainment of the voltage cut-off (3.65 V) is directly correlated with the exceedance of the cyclable capacity defined during the initial configuration. Once the amount of lithium available within this constraint is surpassed, the cell reaches the cut-off potential regardless of the nominal areal capacity specified in the testing regime (Figure S4). This behavior indicates that the initially imposed cyclable threshold is the dominant parameter governing the termination point of the cycle. In the scope of the nucleation and growth study of plated lithium on Cu, each type of sample was deposited with different areal capacities: 0.25, 1, 2 mAh cm^{-2} using a constant current of 1 mA cm^{-2}. The samples were then characterized using SEM.

4.5 | Chemical Reduction on the Cu-CC

The native oxide layer was removed from copper substrates in order to investigate the intrinsic effects of 3D surface architectures and to assess the specific role of copper oxides in determining the material's properties. Three types of samples were employed: pure copper, used as a reference; 3D Cu with parallel line structures (GR5); and 3D Cu surfaces featuring LIPSS. Anhydrous and degassed ethylene glycol (EG, AcroSeal, 99.8%) was employed as the solvent, anhydrous glucose as a mild reducing agent, and anhydrous potassium hydroxide (KOH, Fisher, >85%) as the base. Anhydrous and degassed ethanol (Merck, 99.2%) was used during the final washing steps. The deoxidation treatment was conducted by mixing ethylene glycol, glucose, and KOH in the presence of the copper samples under inert atmosphere conditions to minimize oxygen contamination. The resulting mixture was maintained at approximately 200°C for 4 h. The reaction was performed outside the glovebox due to the elevated temperature requirement. After completion, the system was allowed to cool naturally to room temperature, and the reaction flask was then transferred into the glovebox to prevent reoxidation of the copper surfaces during handling. Inside the glovebox, the copper disks were sequentially rinsed with ethylene glycol and subsequently with ethanol to remove residual reactants and by-products. The cleaned samples were finally dried overnight in a Büchi vacuum drying unit to ensure complete solvent removal. After drying, all samples were stored under an inert atmosphere until further characterization to avoid the formation of new surface oxides.

4.6 | Electrochemical Impedance Spectroscopy (EIS)

Potentiostatic EIS (P-EIS) measurements were performed on a Li-ion full cell LFP versus Cu (modified and not) using a BioLogic MPG2 (Bio-Logic Science Instruments). After an initial formation procedure, the cells were cycled according to a CCCV charge protocol up to 3.65 V, with a constant-voltage step until the current decreased to C/20, followed by discharge at 1 C down to a cutoff voltage of 2.80 V. P-EIS measurements were acquired

26884062, 2026, 4, Downloaded from https://onlinelibrary.wiley.com/doi/10.1002/sstr.202600021 by CochraneItalia, Wiley Online Library on [18/04/2026]. See the Terms and Conditions (https://onlinelibrary.wiley.com/terms-and-conditions) on Wiley Online Library for rules of use; OA articles are governed by the applicable Creative Commons License

every five cycles after a rest period of 10 min, both at 0% and 100% SOC. Impedance spectra were recorded at open-circuit potential by applying a sinusoidal perturbation with an amplitude of 5 mV over a frequency range from 100 kHz to 100 mHz, using 10 points per decade.

4.7 | Scanning Electron Microscope (SEM)

To obtain an overall view of the samples before and after laser treatment, preliminary observations were performed using an optical microscope (Eclipse LV100ND, Nikon, Italy) equipped with five lenses ranging from 5× to 100×, and a digital microscope (VHX, Keyence, Japan) featuring two high-magnification lenses (100–500× and 500–2500×) for 3D surface profiling. For a more detailed examination of surface features, a SEM (Nova NanoSEM 450, FEI, Oregon) was employed to analyze the morphology of the untreated and laser-treated specimens at multiple magnifications.

Electrode morphology was examined at CIC energiGUNE by SEM and energy-dispersive X-ray spectroscopy (EDXS) using an APREO 2 S HiVac microscope operated at 4 kV for imaging and 10 kV for compositional measurements.

Author Contributions

Nassima Yamini: conceptualization (equal), investigation (lead), writing – original draft (lead). **Vincenzina Siciliani:** conceptualization (equal), investigation (equal), methodology (equal), writing – original draft (equal). **Biagio Anderlini:** investigation (supporting), methodology (supporting), writing – original draft (supporting). **Riccardo Pelaccia:** investigation (supporting), methodology (supporting), writing – original draft (supporting). **Marco Borsari:** investigation (supporting), methodology (supporting), writing – original draft (supporting). **Leonardo Orazi:** investigation (supporting), methodology (supporting), writing – original draft (supporting). **Andrea Mescola:** investigation (supporting), methodology (supporting), writing – original draft (supporting). **Francesco De Boni:** investigation (supporting), methodology (supporting), writing – original draft (supporting). **Matteo Lorenzoni:** methodology (equal), writing – review & editing (equal). **Abdolkhaled Mohammedi:** methodology (supporting), project administration (supporting), supervision (supporting), writing – original draft (supporting). **Tommaso Iarocci:** investigation (supporting), methodology (supporting), writing – original draft (supporting). **Luca Bertoli:** investigation (supporting), methodology (supporting), writing – original draft (supporting). **Palanivel Molaiyan:** methodology (supporting), writing – original draft (supporting). **Michal Piszcz:** conceptualization (supporting), methodology (supporting), project administration (supporting), supervision (supporting), writing – original draft (supporting). **Michel Armand:** conceptualization (supporting), investigation (supporting), methodology (supporting), validation (supporting), writing – original draft (supporting). **Vincent Giordani:** conceptualization (equal), methodology (supporting), project administration (supporting), writing – original draft (supporting). **Andrea Paolella:** conceptualization (lead), data curation (lead), investigation (lead), writing – original draft (equal), writing – review & editing (equal).

Acknowledgments

The research activities were supported by Basquevolt (Spain). A. P. would like to thank Prof. Andrea Cornia and Dr. Fabrizio Bernini (UNIMORE, Italy) for their valuable suggestions.

Open access publishing facilitated by Universita degli Studi di Modena e Reggio Emilia, as part of the Wiley - CRUI-CARE agreement.

Funding

The authors have nothing to report.

Conflicts of Interest

The authors declare no conflicts of interest.

Data Availability Statement

The data that support the findings of this study are available from the corresponding author upon reasonable request.

References

1. H. Li, F. Wu, J. Wang, et al., "Anode-Free Sodium Metal Batteries: Optimisation of Electrolytes and Interphases," *Energy & Environmental Science* 18 (2025): 3887.

2. K. R. Ngoy, V. T. Lukong, K. O. Yoro, et al., "Lithium-Ion Batteries and the Future of Sustainable Energy: A Comprehensive Review," *Renewable and Sustainable Energy Review* 223 (2025): 115971.

3. J. Wang, Y. Zhou, Y. Zhuo, et al., "The Challenges and Strategies towards High-Performance Anode-Free Post-Lithium Metal Batteries," *Chemical Science* 16 (2025): 552.

4. B. Yang, H. Wei, H. Wang, et al., "Engineering Moderately Lithiophilic Paper-Based Current Collectors with Variable Solid Electrolyte Interface Films for Anode-Free Lithium Batteries," *Nanomaterials* 14 (2025): 1461.

5. D. Wang, J. Qiu, N. Inui, R. Hagiwara, J. Hwang, and K. Matsumoto, "Between Promise and Practice: A Comparative Look at the Energy Density of Li Metal-Free Batteries and Li Metal Batteries," *ACS Energy Letters* 8 (2023): 5248–5252.

6. Sukanya, F. Bettels, F. Ding, L. Zhang, and R. Wilhelm, "Recycled Graphite Anode from Li-Ion Batteries as Host Material in Li–S Batteries," *ACS Sustainable Resource Management* 2 (2025): 1449–1457.

7. P. Molaiyan, M. Abdollahifar, B. Boz, et al., "Optimizing Current Collector Interfaces for Efficient "Anode-Free" Lithium Metal Batteries," *Advanced Functional Materials* 34 (2024): 2311301.

8. J. Tao, C. Zhang, X. Li, et al., "Advancing Anode-less Lithium Metal Batteries: ZnF_2 Modification and *In Situ* Structural Regulation for Enhanced Performance," *Journal of Materials Chemistry A* 12 (2024): 18127–18136.

9. X. Shi, P. Sun, C. Zhao, et al., "Regulation of Extra Li Inventory in Anode-Free Lithium Metal Batteries by Li-Rich Layered Oxide Cathode Materials," *Nano Letters* 25 (2025): 1623–1629.

10. K. Tang, L. Tian, Y. Zhang, and Z. J. Xu, "Anode-Free Lithium Metal Batteries: A Promising Flexible Energy Storage System," *Journal of Materials Chemistry A* 12 (2024): 16268–16292.

11. D. Petersen, M. Geonenberg, G. Lener, et al "Anode-free Post-Li Metal Batteries" *Materials Horizons* 11 (2024): 5914-5945

12. P. Ma, R. Kumar, K.-H. Wang, and C. V. Amanchukwu, "Active Learning Accelerates Electrolyte Solvent Screening for Anode-Free Lithium Metal Batteries," *Nature Communications* 16 (2025): 8396.

13. M. Abdollahifar and A. Paolella, ""Dead Lithium" Formation and Mitigation Strategies in Anode-Free Li-Metal Batteries," *Batteries & Supercaps* 8 (2025): e202400505.

14. Z. Xie, Z. Wu, X. An, et al., "Anode-Free Rechargeable Lithium Metal Batteries: Progress and Prospects," *Energy Storage Materials* 32 (2020): 386–401.

15. S. Kim, P. N. Didwal, J. Fiates, J. A. Dawson, R. S. Weatherup, and M. D. Volder, "Effect of the Formation Rate on the Stability of Anode-Free Lithium Metal Batteries," *ACS Energy Letters* 9 (2024): 4753–4760.

26884062, 2026, 4, Downloaded from https://onlinelibrary.wiley.com/doi/10.1002/sstr.202600021 by CochraneItalia, Wiley Online Library on [18/04/2026]. See the Terms and Conditions (https://onlinelibrary.wiley.com/terms-and-conditions) on Wiley Online Library for rules of use; OA articles are governed by the applicable Creative Commons License

16. D. Cheng, K. Tran, S. Rao, et al., "Manufacturing Scale-Up of Anodeless Solid-State Lithium Thin-Film Batteries for High Volumetric Energy Density Applications," *ACS Energy Letters* 8 (2023): 4768–4774.

17. Y. An, Y. Zeng, D. Luan, and X. W. Lou, "Materials Design for High-Energy-Density Anode-Free Batteries," *Matter* 7 (2025): 1466–1502.

18. A. Shao, H. Wang, M. Zhang, et al., "Multiscale Interfacial Stabilization via Prelithiation Separator Engineering for Ah-Level Anode-Free Lithium Batteries," *Nature Communications* 16 (2025): 4145.

19. S. Li, F. Wu, T. Chen, et al., "Progress and Challenges for Energy-Dense and Cost-Effective Anode-Free Lithium Metal Batteries," *Energy Material Advances* 6 (2025): 0168.

20. L. Wichmann, S.-K. Jiang, J. H. Tienenkamp, et al., "Origins of Lithium Inventory Reversibility with an Alloying Functional Layer in Anode-free Lithium Metal Batteries," *Nature Communications* 16 (2025): 7216.

21. J. Yang, S. Wang, S. Song, et al., "Cyclable Micron-Sized Silicon-Based Lithium-Ion Batteries at −40°C Enabled by Temperature-Dependent Solvation Regulation," *Advanced Materials* 37 (2025): 2501807.

22. X. Liu, Q. Zhu, A. Jiang, et al., "Realizing a Wide-Temperature Aluminum-Foil-Anode-Based Lithium-Ion Battery," *Advanced Functional Materials* 36 (2026): e21637.

23. W. Yang, A. Chen, P. He, and H. Zhou, "Advancing Lithium Metal Electrode Beyond 99.9% Coulombic Efficiency Via Super-saturated Electrolyte with Compressed Solvation Structure,"*Nature Communications* 16 (2025): 4229.

24. M. Mao, X. Ji, Q. Wang, et al., "Anion-enrichment Interface Enables High-voltage Anode-free Lithium Metal Batteries," *Nature Communications* 14 (2023): 1082.

25. S.-Y. Sun, X.-Q. Zhang, X.-Y. Yan, Z. Zheng, Q.-K. Zhang, and J.-Q. Huang, "Advances in High-Coulombic-Efficiency Lithium Metal Anodes under Practical Conditions in Liquid Electrolytes," *EES Batteries* 1 (2025): 340.

26. A. Mohammadi, P. Ghorbanzade, J. M. Lopez del Amo, L. Monconduit, and L. Stievano, "From Formation to Reactivation of Inactive Lithium in Lithium Metal Anodes," *ChemElectroChem* 12 (2025): e202500242.

27. Q. Zhu, D. Yu, J. Chen, et al., "A 110 Wh Kg−1 Ah-Level Anode-Free Sodium Battery at −40°C," *Joule* 8 (2024): 482–495.

28. L. Yu, X. Tian, M. Zheng, et al., "The Latent Culprit of Anode-Free Lithium Metal Batteries Degradation," *Advanced Functional Materials* 10 (2025): 24486.

29. W. Zhang, A. Paolella, M.-M. Titirici, and T. Tsuchiya, "Advanced Architectures of Electrochemical Interfaces," *Communications Chemistry* 8 (2025): 235.

30. S. T. Oyakhire, W. Zhang, A. Shin, et al., "Electrical Resistance of the Current Collector Controls Lithium Morphology," *Nature Communications* 13 (2022).

31. H. Kwon, J.-H. Lee, Y. Roh, et al., "An Electron-deficient Carbon Current Collector for Anode-free Li-metal Batteries," *Nature Communications* 12 (2021): 5537.

32. G. M. Hobold, J. Lopez, R. Guo, et al., "Moving beyond 99.9% Coulombic Efficiency for Lithium Anodes in Liquid Electrolytes," *Nature Energy* 6 (2021): 951–960.

33. D.-R. Yang, Q. Lai, Y.-T. Long, et al., "Engineering 3D Copper Foam Current Collectors: Modification Strategies and Challenges Toward Stable Lithium Metal Batteries," *Science and Technology of Advanced Materials* 26 (2025): 2525064.

34. J. Lee, Y. Park, J. W. Choi, "Navigating Interfacial Challenges in Lithium Metal Batteries: from Fundamental Understanding to Practical Realization," *Nano Convergence* 12 (2025): 25.

35. Y. Wang, Z. Zhao, J. Zhong, et al., "Hierarchically Micro/Nanostructured Current Collectors Induced by Ultrafast Femtosecond Laser Strategy for High-Performance Lithium-ion Batteries," *Energy & Environmental Materials* 5 (2022): 969–976.

36. E. Ravesio, G. Montinaro, G. Mincuzzi, et al., "Ultrashort Pulsed Laser Texturing of Current Collector for Si/C Li-Ion Anodes: Characterization of Electrochemical Performance and Evolution of Interface Morphology," *Journal of Energy Storage* 109 (2025): 115226.

37. R. Xu, F. Liu, Y. Ye, et al., "A Morphologically Stable Li/Electrolyte Interface for All-Solid-State Batteries Enabled by 3D-Micropatterned Garnet," *Advanced Materials* 33 (2021): 2104009.

38. K.-H. Chen, M. J. Namkoong, V. Goel, et al., "Efficient Fast-Charging of Lithium-Ion Batteries Enabled by Laser-Patterned Three-Dimensional Graphite Anode Architectures," *Journal of Power Sources* 471 (2020): 228475.

39. H. Sun, J. Zhu, D. Baumann, et al., "Hierarchical 3D Electrodes for Electrochemical Energy Storage," *Nature Reviews Materials* 4 (2019): 45–60.

40. J. Park, H. Song, I. Jang, et al., "Three-Dimensionalization via Control of Laser-Structuring Parameters for High Energy and High Power Lithium-Ion Battery under Various Operating Conditions," *Journal of Energy Chemistry* 64 (2022): 93–102.

41. P. Tallone, S. Spriano, D. Versaci, S. Ferraris, A. Tori, and S. Bodoardo, "Picosecond Laser Texturing of Al Current Collector to Improve Cycling Performances and Simplify Recycling of Lithium-Ion Batteries," *Surfaces and Interfaces* 51 (2024): 104659.

42. S. Zhang, G. Yang, X. Li, Y. Li, Z. Wang, L. Chen, "Accommodating Lithium into 3D Current Collectors with a Submicron Skeleton Towards Long-life Lithium Metal Anodes," *Frontiers in Energy Research*,10 (2022): 1013800.

43. A. Tron, A. Beutl, I. Mohammad, and A. Paolella, "Probing the Chemical Stability between Current Collectors and Argyrodite Li6PS5Cl Sulfide Electrolyte," *Communications Chemistry* 8 (2025): 212.

44. Y. Zhao, S. Li, L. Zhu, et al., "Regulating the Donor Number of Solvents for Long-Cycle Anode-Free Lithium Metal Batteries," *Chemical Science* 16 (2025): 14782.

45. J. Lee, H. R. Shin, M. Ryu, et al., "Effect of Stack Pressure on Electrochemical Performance and Uniform Li Plating Feature of Li‖NCM90 Pouch Cells," *Journal of Energy Storage* 118 (2025): 116307.

46. J. Su and C. Huang, "Direct Visualization and Mechanistic Insights into Initial Lithium Plating in Anode-Free Lithium Metal Batteries," *Energy & Environmental Science* 18 (2025): 8815.

47. M. Abdollahifar, A. Paolella, "Anode-Free Batteries: The Energy Density Prize and the Stability Paradox," *ACS Energy Letters* 18 (2025): 1323–1348

48. J.-y. Kim, J.-l. Lee, and J.-w. Lee, "Enabling Stable Li Plating/Stripping Cycles Using a 3D Current Collector Coated with Ag via the Polyol Reduction Process," *Journal of Power Sources* 644 (2025): 236993.

49. S.-B. Xiang, Y. Fu, C. Yin, Y. Hou, H. Tian, and Z. Yin, "Advances in Research on the Inhibitory Effect of 3D Current Collector Structures for Lithium Dendrites," *Inorganic Chemistry Frontiers* 10 (2023): 6767–6791.

50. E. Kim, W. Choi, S. Ryu, Y. Yun, S. Jo, and J. Yoo, "Effect of 3D Lithiophilic Current Collector for Anode-Free Li Ion Batteries," *Journal of Alloys and Compounds* 966 (2023): 171393.

51. O. Garcia-Calvo, A. Gutierrez-Pardo, I. Combarro, et al., "Selection and Surface Modifications of Current Collectors for Anode-Free Polymer-Based Solid-State Batteries," *Frontiers in Chemistry* 10 (2022): 934365.

52. C.-J. Huang, B. Thirumalraj, H.-C. Tao, et al., "Accomodating Lithium into 3D Current Collectors with a Submicron Skeleton Towards Long-life Lithium Metal Anodes," *Nature Communications* 12 (2021): 1452.

26884062, 2026, 4, Downloaded from https://onlinelibrary.wiley.com/doi/10.1002/sstr.202600021 by CochraneItalia, Wiley Online Library on [18/04/2026]. See the Terms and Conditions (https://onlinelibrary.wiley.com/terms-and-conditions) on Wiley Online Library for rules of use; OA articles are governed by the applicable Creative Commons License

53. Y. Zhao, S. Li, Y. Liu, et al., "Artificial Cells Capable of NO Generation with Light Controllable Membraneless Organelles for Melanoma Therapy," *Advanced Materials* 37 (2025): 2500242.

54. D. Aurbach and A. Zaban, "Impedance Spectroscopy of Lithium Electrodes," *Journal of Electroanalytical Chemistry* 348 (1993): 155–179.

55. M. A. Zabara, G. Kat1rc1, and B. Ulgut, "Operando Investigations of the Interfacial Electrochemical Kinetics of Metallic Lithium Anodes via Temperature-Dependent Electrochemical Impedance Spectroscopy," *The Journal of Physical Chemistry C* 126 (2022): 10968–10976.

56. D. Aurbach, A. Zaban, Y. Gofer, et al., "Recent Studies of the Lithium-Liquid Electrolyte Interface Electrochemical, Morphological and Spectral Studies of a Few Important Systems," *Journal of Power Source* 54 (1995): 76–86.

57. D. Aurbach, "Review of Selected Electrode–solution Interactions which Determine the Performance of Li and Li Ion Batteries," *Journal of Power Sources* 89 (2000): 206–218.

58. M. S. Whittingham, "Ultimate Limits to Intercalation Reactions for Lithium Batteries," *Chemical Reviews* 114 (2014): 11414–11443.

59. H. Li, G. Wang, J. Hu, J. Li, J. Huang, and S. Xu, "Laser-Constructing 3D Copper Current Collector with Crystalline Orientation Selectivity for Stable Lithium Metal Batteries," *Energy & Environmental Materials* 7 (2024): e12768.

60. M. Ratynski, M. Krajewski, T. Tamulevicius, et al., "Femtosecond Laser Treatment of Copper Current Collectors and Their Application in Li-Ion Batteries," *ACS Applied Engineering Materials* 3 (2025): 3228–3238.

61. A. Mohammadi, A. Hagopian, S. Sayegh, et al., "Towards Understanding the Nucleation and Growth Mechanism of Li Dendrites on Zinc Oxide-Coated Nickel Electrodes," *Journal of Materials Chemistry A* 10 (2022): 17593–17602.

62. S. Menkin, C. A. O'Keefe, A. B. Gunnarsdottir, et al., "Toward an Understanding of SEI Formation and Lithium Plating on Copper in Anode-Free Batteries," *The Journal of Physical Chemistry C, Nanomaterials and Interfaces* 125, no. 30 (2021): 16719–16732.

63. N. Li, T. Jia, Y. Liu, S. Huang, F. Kang, and Y. Cao, "Rational Engineering of Anode Current Collector for Dendrite-Free Lithium Deposition: Strategy, Application, and Perspective," *Frontiers in Chemistry* 10 (2022): 884308.

64. J. Luan, Q. Zhang, H. Yuan, et al., "Plasma-Strengthened Lithiophilicity of Copper Oxide Nanosheet–Decorated Cu Foil for Stable Lithium Metal Anode," *Advanced Science* 6 (2019): 1901433.

65. C. Toigo, M. Frankenberger, N. Billot, et al., "Improved Li4Ti5O12 Electrodes by Modified Current Collector Surface," *Electrochimica Acta* 392 (2021): 138978.

66. Y. Wang, B. Jose, Y. Yuan, et al., "Revealing the Neglected Role of Passivation Layers of Current Collectors for Solid-State Anode-Free Batteries," *Advanced Materials* 37 (2025): e13090.

67. C-P. Yang, Y-X. Yin, S-F. Zhang, N-W. Li, Y-G. Guo, "Decoupling the origins of irreversible coulombic efficiency in anode-free lithium metal batteries," *Nature Communications* 12 (2015): 1452.

Supporting Information

Additional supporting information can be found online in the Supporting Information section. **Supporting Fig. S1:** 3D profile of LIPSS on copper using an optical profilometer: the maximum difference in height refers to the waviness of the entire sheet analyzed; where LIPSS are present, no significant differences in height are detected. **Supporting Fig. S2:** 3D profile of LIPSS on copper under an Atomic Force Microscope: a) topography of the 40x40 μm sample, showing a root mean square roughness of approximately 70 nm; b) 2D FFT of the image; c) profile of the diagonal, showing the pitch of the LIPSS structures of approximately 1.07 μm, calculated as the inverse of the dominant spatial frequency starting from the center. The laser trace mark with a pitch of 4.5 μm is also clearly visible. **Supporting Fig. S3:** Coin cell format. **Supporting Fig. S4:** $LiFePO_4$ voltage profile for each capacity for the 2nd cycle after formation (discharge). **Supporting Fig. S5:** Diffraction pattern profile of the CCs before - samples **a)**, **c) e)** – and after – samples **b)**, **d)**, **f)** – the etching process. In the figure g) is represented the enlarged region between where two weak impurity diffraction peaks were detected at $2\theta \approx 39°$ and around 45°. **Supporting Fig. S6:** High-resolution O 1s XPS spectrum of the samples before and after the etching process, with deconvoluted components corresponding to Cu–O bonding and surface contamination (C–O) shown. **Supporting Fig. S7:** High-resolution XPS spectra of the Cu 2p region (left, Cu2D-a, GR5-c, LIPSS-e) and the Cu LMM Auger region (right, Cu2D-b, GR5-d, LIPSS-f) for the samples before the etching process, with the characteristic core-level and Auger peaks displayed as a function of binding energy. **Supporting Fig. S8:** High-resolution XPS spectra of the Cu 2p region (left, D_Cu2D-g, D_GR5-i, D_LIPSS-m) and the Cu LMM Auger region (right, D_Cu2D-h, D_GR5-l, D_LIPSS-n) for the samples after the etching process, with the characteristic core-level and Auger peaks displayed as a function of binding energy. **Supporting Fig. S9:** Graphical scheme used to extrapolate R_s and Re_{peak} from the Nyquist plots at 12 h, employed for the qualitative estimation of the interfacial arc resistance without equivalent-circuit fitting. **Supporting Fig. S10:** Ex situ SEM images of Li plating morphology on laser-textured GR5 Cu and planar Cu (Cu2D) at increased plated areal capacity. (a) GR5 after plating 1 mAh cm^{-2} (top-view). (b,c) GR5 after plating 2 mAh cm^{-2} at low and high magnification, respectively. (d,e) Cu2D after plating 2 mAh cm^{-2} at low and high magnification, respectively. At higher plated capacity, deposits become more compact and increasingly cover/fill the available surface features, consistent with progressive filling of the 3D texture and partial convergence toward a more planar-like surface morphology. Scale bars as indicated in each panel. **Supporting Table S1:** Laser parameters for laser texturing 10 μm copper foil.

26884062, 2026, 4, Downloaded from https://onlinelibrary.wiley.com/doi/10.1002/sstr.202600021 by CochraneItalia, Wiley Online Library on [18/04/2026]. See the Terms and Conditions (https://onlinelibrary.wiley.com/terms-and-conditions) on Wiley Online Library for rules of use; OA articles are governed by the applicable Creative Commons License